ONLINE FIRST

This is a provisional PDF only. Copyedited and fully formatted versión will be made available at final publication

HISTOLOGY AND HISTOPATHOLOGY

ISSN: 0213-3911
e-ISSN: 1699-5848

Submit your article to this Journal (http://www.hh.um.es/Instructions.htm)

Colorectal cancer histopathology image analysis: a comparative study of prognostic values of automatically extracted morphometric nuclear features in multispectral and red-blue-green imagery

Authors: Wenlou Liu, Aiping Qu, Jingping Yuan, Linwei Wang, Jiamei Chen, Xiuli Zhang, Hongmei Wang, Zhengxiang Han and Yan Li

DOI: 10.14670/HH-18-715
Article type: ORIGINAL ARTICLE
Accepted: 2024-01-23
Epub ahead of print: 2024-01-23

Colorectal cancer histopathology image analysis: a comparative study of prognostic values of automatically extracted morphometric nuclear features in multispectral and red-blue-green imagery

Running head: Multispectral imaging in colorectal cancer

Wenlou Liu, MD [1,†], Aiping Qu, MD [2,†], Jingping Yuan, MD [3], Linwei Wang, MD [4], Jiamei Chen, MD [5], Xiuli Zhang, MD [6], Hongmei Wang, MD [1], Zhengxiang Han, MD [1,*], Yan Li, MD [7,*]

[1] Department of Oncology, Affiliated Hospital of Xuzhou Medical University, Xuzhou 221002, China.

[2] School of Computer, University of South China, Hengyang 421001, China.

[3] Department of Pathology, Renmin Hospital of Wuhan University, Wuhan 430071, China.

[4] Department of Oncology, Zhongnan Hospital of Wuhan University, Wuhan 430071, China.

[5] Department of Oncology, Renmin Hospital of Wuhan University, Wuhan 730071, China.

[6] Department of Radiology, Affiliated Hospital of Xuzhou Medical University, Xuzhou 221002, China.

[7] Department of Cancer Surgery, Beijing Tsinghua Changgung Hospital, Tsinghua University, Beijing 102218, China.

[†]Wenlou Liu and Aiping Qu contributed equally to this work.

[*] **Correspondence:**

Prof. Zhengxiang Han, PhD, Department of Oncology, The Affiliated Hospital of Xuzhou Medical University, Xuzhou 221002, China. E-mail: cnhzxyq@163.com.

Prof. Yan Li, PhD, Department of Cancer Surgery, Beijing Tsinghua Changgung Hospital, Tsinghua University, No. 168 Litang Road, Changping District, Beijing 102218, China. Tel: +86-10-56112345, E-mail: liyansd2@163.com

Abstract

Objectives: Multispectral imaging (MSI) has been utilized to predict the prognosis of colorectal cancer (CRC) patients, however, our understanding of the prognostic value of nuclear morphological parameters of bright-field MSI in CRC is still limited. This study was designed to compare the efficiency of MSI and standard red-green-blue (RGB) images in predicting the prognosis of CRC.

Methods: We compared the efficiency of MS and conventional RGB images on the quantitative assessment of hematoxylin-eosin (HE) stained histopathology images. A pipeline was developed using a pixel-wise support vector machine (SVM) classifier for gland-stroma segmentation, and a marker-controlled watershed algorithm was used for nuclei segmentation. The correlation between extracted morphological parameters and the five-year disease-free survival (5-DFS) was analyzed.

Results: Forty-seven nuclear morphological parameters were extracted in total. Based on Kaplan-Meier analysis, eight features derived from MS images and seven featured derived from RGB images were significantly associated with 5-DFS, respectively. Compared with RGB images, MSI showed higher accuracy, precision, and Dice index in nuclei segmentation. Multivariate analysis indicated that both integrated parameters 1 (factors negatively correlated with CRC prognosis including nuclear number, circularity, eccentricity, major axis length) and 2 (factors positively correlated with CRC prognosis including nuclear average area, area perimeter, total area/total perimeter ratio, average area/perimeter ratio) in MS images were independent prognostic factors of 5-DFS, in contrast with only integrated parameter 1 ($P < 0.001$) in RGB images. More importantly, the quantification of HE-stained MS images displayed higher accuracy in predicting 5-DFS compared with RGB images (76.9% vs 70.9%).

Conclusions: Quantitative evaluation of HE-stained MS images could yield more information and better predictive performance for CRC prognosis than conventional RGB images, thereby contributing to precision oncology.

Keywords: colorectal cancer; multispectral imaging; histopathology image analysis; segmentation; prognosis

INTRODUCTION

Colorectal cancer (CRC), ranked as the third most common cancer, is considered one of the leading causes of cancer-related death worldwide (Hossain *et al.*, 2022). There is a predicted rise in the number of CRC cases, showing an expected increase of 60% in incidence by 2030 (Wong *et al.*, 2021). Traditionally, the diagnosis of CRC mainly relied on histopathological examination as certain histological features (e.g. pathological grade) have been reported to be associated with its pathogenesis and progression (Dolens *et al.*, 2021). However, qualitative assessment of histopathological features is not sufficient for predicting the prognosis of CRC. Besides, it is still a challenge to achieve inter- and intra-observer agreement and reproducibility of tumor grading (Rathore *et al.*, 2014).

With the advances in digital pathology and high-throughput technology, computer-aided image (CAI) has been adopted in CRC diagnosis and grading (He *et al.*, 2012; Kudo *et al.*, 2021). Various CAI-based algorithms and approaches have been proposed for object segmentation, feature extraction, malignancy classification, and computer-aided grading and prognosis of CRC (Komura and Ishikawa, 2018). The image quality will affect the detection of the region of interest (ROI), as well as the precision of the object segmentation. It has been acknowledged that image quality and color variation could directly affect the efficiency of CAI analysis (Tani *et al.*, 2012; Bai *et al.*, 2023). Thus, it is essential to obtain high-quality hematoxylin-eosin (HE) images for the quantitative evaluation of CRC grading and prognosis.

Multispectral imaging (MSI), as an advanced imaging modality widely utilized in pathology(Waterhouse *et al.*, 2023), can capture high-resolution images with accurate spectral and spatial information. To date, extensive studies have focused on the application of MSI to HE histological image analysis. For instance, Zhang *et al*. indicated that spectral images contained more information on cancer classification than red-green-blue (RGB) images (Zhang *et al.*, 2022). In addition, in a meta-analysis involving the utility of MSI for cancer diagnosis, MSI data exploitation was superior to RGB images for cancer diagnosis (Ortega *et al.*, 2020). Furthermore, Siegel *et al*. reported that MSI showed the potential for the noninvasive detection of malignancies (Siegel *et al.*, 2018). They indicated that the MSI for colon tissue biopsy classification provided promising visual results of segmentation.

MSI is promising in the automated quantitative evaluation of histopathology images, contributing to the diagnosis and classification of CRC (Hoyt, 2021). It is still necessary to explore the additional benefits of MSI in routine HE image analysis, especially the values of computerized morphological features for prognostic predictors. To date, little is known about the prognostic value of morphological nuclear features of bright-field MSI in CRC patients. In a previous study, a novel algorithm was proposed for the automatic analysis of HE histopathological

images from breast invasive ductal carcinoma (IDC), which screened additional prognostic factors for prognosis prediction in IDC patients (Chen *et al.*, 2015). In this study, we employed MSI and conventional RGB images for the automatic extraction of the objective quantitative nuclear morphological features from the pixel and object levels. Then we investigated the correlation between these parameters and five-year disease-free survival (5-DFS) and compared the efficiency of MSI and RGB images in predicting the prognosis of CRC.

MATERIALS AND METHODS

Patients and samples

In this retrospective analysis, we included 134 CRC patients who underwent curative surgical resection between 2009 and 2011 in the Department of Pathology, Zhongnan Hospital, Wuhan University. The inclusion criteria were as follows: those with CRC confirmed after histopathological analysis; and those with a follow-up of at least five years. Patients who received chemotherapy or radiotherapy prior to surgical resection or those with incomplete medical files were excluded from this study. Each patient signed the informed consent. The protocols of this study were approved by the Ethical Committee of Zhongnan Hospital, Wuhan University. TNM staging and histological grade were evaluated according to the sixth edition of the American Joint Committee on Cancer (AJCC) TNM system (Sobin *et al.*, 2010) and the fourth edition of the WHO histological grade (Bosman *et al.*, 2010). The design and flowchart of this study are presented in **Figure 1**.

HE staining

Collected tissues were fixed with formalin, followed by embedding in paraffin. Then, sections (4 μm) were mounted onto glass slides. HE staining was performed as previously described (Fischer *et al.*, 2008).

Image acquisition

HE-stained slices were observed under an Olympus BX52 bright-field microscope equipped with an Olympus DP72 RGB Microscope Digital camera (Olympus Optical, Tokyo, Japan) and the Nuance MSI system (Cambridge Research and Instrumentation, Woburn, MA, USA). ROIs in HE images with characteristics of invasive adenocarcinoma were selected under a magnification of ×100 after excluding the necrotic area and adenoma lesions. Each ROI with tumor epithelial cells and stromal cells was captured under a magnification of ×40 based on unified acquisition parameters as previously described (Liu *et al.*, 2016). To minimize selection bias, six high-power field (HPF) images were randomly selected from the ROIs of each slide. For multispectral images, six

spectral cubes with complete spectral information at 20-nm wavelength intervals and those with an optimal spectral segment between 420 nm and 720 nm were randomly obtained from different areas of the sections. A total of 1,608 bright-field HE images (i.e., 804 RGB and 804 MS images) were captured and saved in a tagged image file format (TIFF), with a consistent resolution of 1,360×1,024 pixels, for further analysis.

Image processing and feature extraction

To extract image features related to prognosis, histological structures were automatically identified and segmented by an image recognition technique. The processing for RGB and multispectral images consisted of preprocessing, segmentation, postprocessing, and feature extraction (Qu *et al.*, 2014).

A two-step pipeline was utilized for the segmentation of the glands-stroma and nuclear components in each image. For the segmentation of glands-stroma, pixel-level color features were extracted based on a local homogeneity model (Kaushal *et al.*, 2022), while pixel-level Haralick texture features were calculated with the fast parallelized segmentation method (Stegmaier *et al.*, 2014). The boundary of each glandular object on the visual field was delineated by a qualified pathologist. Then the support vector machine (SVM) model was constructed with randomly selected labeled pixels. Finally, the glandular and stroma structures of all the images were segmented with the SVM classifier. For nuclei segmentation, we proposed a marker-controlled watershed segmentation method to identify the nuclei from different images (e.g., nuclei of epithelial cells and interstitial lymphocytes) as previously described (Qu *et al.*, 2014).

As segmentation showed a lack of robustness to noise and could not classify all pixels to the objects accurately, image identification was aided by a qualified pathologist (Yuan JP) to eliminate incorrect segmentations. Finally, pixel- and object-levels of morphological features were extracted.

Statistical analysis

Before statistical analysis, X-tile software was utilized for the conversion of nuclear morphological parameters to ordinal data as previously described (Camp *et al.*, 2004). Then, univariate survival analysis was used to set the best cutoff value and the number of patients of various degrees. The Kaplan-Meier method was used for dimensionality reduction of the features. Kaplan-Meier curves were utilized to analyze the correlation between morphological features, conventional pathological prognostic factors, and 5-DFS, while the significance among subgroups was analyzed by the log-rank test. A multivariate Cox proportional hazards regression model was performed to identify the independent prognostic factors of CRC. Sensitivity, specificity, positive predictive values

(PPVs), and negative predictive values (NPVs) for predicting CRC recurrence were calculated. The receiver operating characteristic (ROC) curve was used to determine the predictive value of the features of interest. The Chi-square test was used to compare the predictive accuracy of MSI and RGB images, and the confidence intervals of the difference were determined. Statistical analyses were performed with SPSS version 19.0 (Chicago, IL, USA). A *P* value of less than 0.05 was considered to be statistically significant.

RESULTS

Major clinicopathological characteristics

Demographic and clinicopathological characteristics of the 134 CRC patients are presented in **Table 1**. The median age was 62.6 years (33-91). The 5-DFS rate was 63.4% with a median DFS of 48.2 months. In the study cohort, 33 patients (24.6%) were diagnosed with local recurrence and 16 (11.9%) presented distant metastases. The corresponding bright-field MSI and RGB images of HE-stained histopathological images were acquired, and representative images are shown in **Fig 2**. MSI displayed better image qualities than conventional RGB images, which was beneficial for further computer analysis.

Image segmentation evaluation

To compare the segmentation capacity of the two methods, we randomly selected 12 pairs of RGB and MS images from 12 patients (grade I: four patients; grade II: four patients; grade III: four patients) to construct standard datasets. Based on manual segmentation, 12 independent sets were implemented to test the corresponding classifiers. However, challenges remained in distinguishing the nuclei of epithelial cells or the nuclear boundary in poorly differentiated or nucleus-overlapping regions.

A marker-controlled watershed algorithm was utilized to segment the nucleus. A much stricter pixel-based quantitative evaluation was performed by automatically comparing computer outputs with the manually segmented imaging data. Then, the accuracy, sensitivity, specificity, precision, and object-level Dice index for the segmentation of each corresponding RGB and MS image were determined according to the specific calculation formulas as previously described (Qu *et al.*, 2014; Sirinukunwattana *et al.*, 2017). Compared with RGB images, the proposed MSI method had higher accuracy (88.6% vs. 84.5%), precision (69.7% vs. 65.2%), and Dice index (0.650% vs. 0.593%) in pixel-based nuclei segmentation (**Table 2**). To further evaluate the segmentation performance, we compared the segmentation results of the well, moderately, and poorly differentiated CRCs between RGB and MS images **(Fig 3)**.

Feature extraction and grading

Based on computer-aided automatic segmentation of the images **(Fig 4)**, 115 image features were extracted from RGB and MS images. These features could be classified into pixel-level features (n=68), which included color and texture parameters, and object-level features (n=47) which included nuclear morphometry (object size and shape) and topological parameters (**Supplementary Table 1**). Due to the unclear biological significance, the pixel-level features were not analyzed. Then, X-tile software based on the best *P* value was adopted to automatically judge the cut-off points of the object-level features, followed by categorizing each measured parameter into grade I, grade II, or grade III, respectively. Subsequently, univariate survival analysis was employed for dimensionality reduction of all features to screen out the significant image features. The results demonstrated that eight nuclear features extracted from MS images and seven from RGB images were significantly associated with 5-DFS (all $P < 0.05$, **Tables 3** and **4**).

Association of nuclear morphometric parameters with 5-DFS

Survival analysis was conducted to investigate the association between the 5-DFS of CRC patients and nuclear morphometric parameters extracted from MSI and RGB images. For MS images, 5-DFS was negatively correlated with nuclear number ($P<0.001$), circularity ($P<0.001$), eccentricity ($P=0.002$), and major axis length ($P=0.001$) (**Fig. 5**). In addition, for RGB images, 5-DFS was negatively correlated with nuclear number ($P<0.001$), circularity ($P<0.001$), eccentricity ($P=0.005$), and major axis length ($P=0.003$) (**Fig. 6**). For both RGB and MS images, 5-DFS was positively correlated with the nuclear average area (all $P<0.001$), perimeter area (MSI: $P=0.005$, RGB: $P=0.009$), total area/total perimeter ratio (MSI: $P=0.003$, RGB: $P=0.006$). 5-DFS was positively correlated with the average (area/perimeter) ratio based on MS images ($P=0.002$) rather than RGB images ($P=0.104$).

The number, circularity, and average area obtained from MSI could distinguish 5-DFS into three categories with statistical differences between them (**Figs. 5a, b, and e**). However, for RGB images, only number and circularity could distinguish 5-DFS into separate categories with statistical differences (**Figs. 6a and b**). All these indicated that CAI analysis based on MSI presented better performance than RGB images in discriminating the prognosis of CRC patients.

Prognostic values of nuclear morphometric and integrated parameters

ROC analysis was implemented to further evaluate the prognostic values of nuclear parameters with statistical significance. For MSI, the number, circularity, eccentricity, and major axis length were negatively correlated with 5-DFS with areas under the curve (AUC) of > 0.5. The average area, average perimeter, total area/total perimeter, and average (area/perimeter) were positively correlated with 5-DFS with an AUC of < 0.5. In RGB images, only three parameters (i.e. average area, average perimeter, total area/total perimeter) were positively correlated with 5-DFS. All features statistically correlated with 5-DFS, and the prognostic values of MS images for 5-DFS were higher than those of RGB images (all P<0.05, **Table 5**).

Subsequently, these parameters were attributed corresponding scores according to their grades (grade I = 1 score; grade II = 2 score; and grade III = 3 score), and were pooled into integrated parameter 1 and integrated parameter 2. Then, integrated parameters 1 and 2 were classified into low, moderate, and high levels by X-tile software. ROC analysis indicated that integrated parameter 1 in MS images had higher AUCs than the four independent parameters that were negatively correlated with prognosis; integrated parameter 2 had lower AUCs than the four independent features that were positively correlated with prognosis (**Fig 7a**). Similar results were also revealed in the analysis of RGB images (**Fig 7b**). Additionally, the prognostic value of integrated parameter 1 in MS images (AUC = 0.785; 95% CI, 0.700-0.870; P<0.001) was greater than that in RGB images (AUC = 0.773; 95% CI, 0.691-0.855; P<0.001). Similar results were also obtained in the analysis of integrated parameter 2 (**Table 5**).

Validation of integrated parameters by multivariate analysis

To further investigate the prognostic efficiency of the newly identified integrated parameters for CRC prognosis, multivariate analysis was performed coupling with integrated parameter 1, integrated parameter 2, and traditional prognostic parameters. Multivariate analysis showed four independent prognostic factors of CRC in MSI, including lymph node (LN) status (P < 0.001), integrated parameter 1 (P<0.001), integrated parameter 2 (P<0.001), and clinical stage (P=0.009). In RGB images, LN status (P<0.001), integrated parameter 1 (P<0.001), and clinical stage (P=0.002) were independent prognostic factors of CRC (**Table 6**). Moreover, the weighted analysis of nuclear integrated parameter 1 for predicting 5-DFS was carried out. The hazard ratio (HR) of integrated parameter 1 of MS images (HR = 2.863; 95% CI, 2.014-4.070) was higher than clinical stage (HR = 2.457; 95% CI, 1.248-4.835), but lower than LN status (HR = 5.165; 95% CI, 2.529-10.550). However, the HR of integrated parameter 1 from RGB images was lower than LN status (HR = 2.761; 95% CI, 1.881-4.052 vs HR = 4.490; 95% CI, 2.204-

9.149) and clinical stage (HR = 2.761; 95% CI, 1.881-4.052 vs HR = 2.968, 95% CI, 1.491-5.911). In addition, the HR of integrated parameter 1 in MS images was higher than that in RGB images (HR = 2.863; 95% CI, 2.014-4.070 vs HR = 2.716, 95% CI; 1.881-4.052; **Table 6**).

Evaluation of prediction efficiency of nuclear integrated parameters

In terms of analysis of integrated parameter 1, compared with RGB images, MSI showed a higher sensitivity (75.5% vs 63.3%), specificity (77.6% vs 75.3%), PPV (66.1% vs 59.6%), and NPV (84.6% vs 78.0%) for the prediction of CRC prognosis, with no statistical significance (**Table 7**). Moreover, the predictive accuracy for recurrence obtained from MSI was significantly higher than that from RGB images (76.9% vs 70.9%, *P*=0.041; 95% CI: 1.04-13.90%). Similarly, in terms of analysis of integrated parameter 2, the predictive accuracy for recurrence obtained from MSI was significantly higher than that from RGB images (73.9% vs 64.9%, *P*=0.007; 95% CI: 3.0-16.4%).

DISCUSSION

In the present study, we proposed an advanced CAI processing technique to quantitatively evaluate bright-field MSI for the prediction of CRC prognosis. To our knowledge, this is the first study on predicting the prognosis of CRC patients by quantitatively analyzing morphological features from HE-stained histopathology images. Herein, we designed an automated workflow that identified objective parameters from HE-stained MS and conventional RGB images, and then we utilized the machine-learning classifiers to predict the survival of CRC patients. This method for the quantification of MS images was superior in predicting CRC prognosis than that of RGB images. Combined with our previous work on MSI in IHC analysis (Liu *et al.*, 2016), we concluded that MSI has potential as a standard and optimal digital imaging system for the diagnosis and prediction of CRC prognosis.

The advantages of MSI include wide-field imaging with spectroscopy and noninvasive, nonionizing tissue analysis without contrast agents (Wu *et al.*, 2022). MS images showed more spectral channels and higher spectral resolution than RGB images, which might aid in extracting more useful information on pathology (Irshad *et al.*, 2014; Fereidouni *et al.*, 2018). Moreover, MSI captured the spectral images of a large area of tissues, overcoming the under-sampling problem associated with spectroscopy and biopsy (Buchberger *et al.*, 2018). In this study, we employed RGB imaging and an MSI system in CRC cohorts and compared their efficiency in predicting prognosis. Our data indicates that MS images provide better overall image qualities and more useful information than RGB images.

The spectral information in MSI data enabled the characterization, identification, and classification of

different types of tissues. However, the quantitative analysis of spectral data is still a computational challenge due to the presence of a large data volume, including the high dimensionality of spectral bands, visible wavelength range, and high spatial resolution (Halicek *et al.*, 2019). Computational image analysis methods could quickly extract information from tumor tissue sections, which significantly improved the objectivity and accuracy of image quantitative determination (Wang *et al.*, 2016). Previous literature reported that spectral data generated with MSI can also be automatically excavated to extract more useful diagnostic information for cancer classification by CAI (Liang *et al.*, 2022). For instance, Chaddad *et al*. proposed a classification based on Haralick's texture features generated from segmented MS images, which were effective in discriminating three types of CRC cells (Chaddad *et al.*, 2011).

Algorithms for automated gland segmentation in digitized images of HE-stained CRC tissue slides contributed to the detection of cancer grade and increased reproducibility of grading (Rathore *et al.*, 2019). Additionally, automated nuclei segmentation is a prerequisite for various quantitative analyses, including automatic morphological feature computation (Stegmaier *et al.*, 2014). However, it is difficult to precisely separate the nuclei as HE-stained histopathology images are complex in nature. In this study, we proposed a method based on the marker-controlled watershed for cell nucleus segmentation, and then compared the segmentation capacity in RGB and MS images. The results showed that MS images presented higher accuracy, precision, and Dice index values in pixel-based nuclei segmentation than RGB images. This demonstrated that the quantitative analysis of MS images could be a promising candidate for extracting morphological features in the future.

CAI techniques have been reported to be effective in predicting the prognosis of cancers (Gao *et al.*, 2019; Xu *et al.*, 2023). Malshy *et al*. utilized computerized nuclear morphometry to distinguish different grades and predict the prognosis of CRC (Malshy *et al.*, 2022). Wang *et al*. reported the prognostic values of CAI features in the triple negative (TN) and stromal components associated with the prognosis of breast cancer (Wang *et al.*, 2022). In our study, we tried to extract a set of morphological nuclear parameters correlated with prognosis in HE-stained MS and RGB images of CRC. With 5-DFS as the golden criterion to judge their clinical significance, we found that more nuclear morphological parameters extracted from MS images were significantly correlated with 5-DFS. Moreover, CAI for MS images was superior in determining the risk levels than that for RGB images. ROC analysis indicated four parameters with AUC >0.5 and another four parameters with AUC <0.5 in MS images for predicting the prognosis of CRC; there were only three parameters with AUC <0.5 in RGB images. Then, we further evaluated the prognostic values of integrated parameters by multivariate analysis. In MS images, integrated parameters 1 and 2 were identified as independent prognostic factors for 5-DFS, however, in RGB images, only

integrated parameter 1 was identified as an independent risk factor. This implied that morphological nuclear parameters of MS images had higher prognostic values in predicting the prognosis of CRC than that of RGB images. Furthermore, integrated parameter 1 derived from MS images had even higher predictive effectiveness on 5-DFS than histological grade and clinical stage. More importantly, compared with RGB images, MS images displayed better accuracy for predicting CRC recurrence. Our results show that the model based on the integrated parameters of MS images could more effectively predict 5-DFS than conventional RGB images. Thus, MS images were more suitable for prognostic prediction, benefitting from better performances in identifying CRC subgroups and recurrence prediction.

There are some limitations to this study. Firstly, the results should be further evaluated in a larger multicenter CRC population to reduce the systematic bias of any single image source. Secondly, this study only analyzed prognostic factors from nuclear morphological parameters, without covering the prognostic values of color and texture features, mitotic activity, and tumor microenvironment in the corresponding RGB and MS images of CRC related to prognosis (Veta *et al.*, 2016). Thirdly, we only evaluated the relationships between nuclear parameters and the prognosis of CRC patients by 5-DFS and did not evaluate overall survival. Finally, further prospective clinical studies are required to validate the prognostic values of the independent predictors in conventional RGB and MS images.

In conclusion, we developed a novel approach for the assessment of HE images by automatically quantifying morphometric parameters of MS images and validated the potential of MSI in predicting prognoses in CRC patients. Quantitative analysis of HE-stained MS images was superior to conventional RGB images in predicting the prognosis of CRC.

Funding

This study was funded by the Key Project of the National Natural Science Foundation of China (No. 81230031/H18), Project of the Affiliated Hospital of Xuzhou Medical University (No. 2020KB006), and China Postdoctor Science Foundation (No. 2020M670078ZX).

Conflict of interest

The authors declare that they have no conflict of interest.

Ethics approval

All procedures performed in studies involving human participants were in accordance with the ethical standards of the institutional and/or national research committee and with the 1964 Helsinki Declaration and its later amendments or comparable ethical standards. The study protocols were approved by the Ethical Committee of The Affiliated Hospital of Xuzhou Medical University (XYFY2023-KL076-02).

Informed consent

Informed consent was obtained from all individual participants included in the study.

Author contribution

Wenlou Liu: Data curation, formal analysis, software, writing-original draft. Aiping Qu: Data curation, methodology, validation, writing-original draft. Jingping Yuan: Methodology, formal analysis, resources. Linwei Wang: Data curation, software. Jiamei Chen: Visualization, resources. Xiuli Zhang: Visualization, resources. Hongmei Wang: Data curation. Zhengxiang Han: Conceptualization, formal analysis, writing – review and editing. Yan Li: Conceptualization, formal analysis, writing – review and editing.

Data availability statement

The data that support the findings of this study are available from the corresponding author upon reasonable request.

Figure legends

Fig 1. The design and main technical procedures of the study. (**a**) HE-stained tissue sections slides were prepared from formalin-fixed paraffin-embedded tissue blocks of 134 CRC patients. (**b**) The digital images corresponding to HE-stained RGB and MS images were captured by a conventional charge-coupled device (CCD) and MS imaging system. (**c**) The major steps of computer-aided image (CAI) analysis. (**d**) The quantitative outputs of all extracted features were divided into three grades by X-tile software and analyzed by the Kaplan-Meier method. CRC, colorectal cancer; SVM, support vector machine.

Fig 2. HE-stained histopathological images of CRC. (**a-c**) Conventional RGB images of well-differentiated, moderately differentiated, and poorly differentiated adenocarcinoma. (**d-f**) The corresponding MS images of well-differentiated, moderately differentiated, and poorly differentiated adenocarcinoma. Magnification ×400; scale bar: 20 μm for all images.

Fig 3. Evaluation outputs of nuclei segmentation on RGB and MS images of HE-stained CRC histopathological images. (a-f) The first column shows the original RGB and MS images of HE-stained well-differentiated, moderately differentiated, and poorly differentiated CRC. (a1-f1) The second column shows the ground truth images labeled by a qualified pathologist and nuclei were labeled with dark green boundaries. (a2-f2) The third column shows the results of nuclei segmentation images obtained by the proposed method and nuclei were labeled with green boundaries. (a3-f3) The fourth column presents evaluation outputs of segmentation in the form of pseudo-color images. Yellow, epithelial region; black, stroma matrix; red, epithelial cell nuclei; green, stroma cell nuclei. Magnification: ×400; scale bar: 20 μm.

Fig 4. The results of image processing by CAI and RGB images. (**a**) Histopathologic HE-stained CRC image. (**b**) Image pre-processing to improve quality. (**c**) The segmentation of SVM classification. The glandular lumens were labeled with green boundaries. (**d**) Nuclei segmentation by marker-controlled watershed algorithm. The deep-green region represents an individual nuclear region. (**e**) Integration of glands-stroma and nuclei segmentation results. (**f**) All image objects were sub-classified in the form of pseudo-color images after segmentation (yellow, glandular lumens region; black, stroma matrix; red, epithelial cell nuclei; green, stroma cell nuclei). Magnification: ×400; scale bar: 20 μm. SVM, support vector machine.

Fig 5. Relationship between nuclear morphometric parameters extracted from MS images and 5-DFS of CRC patients. Among the eight features, number (a), circularity (b), eccentricity (c), and major axis length (d) were negatively correlated with 5-DFS. The average area (e), average perimeter (f), total (area/perimeter) ratio (g), and average (area/perimeter) ratio (h) were positively correlated with 5-DFS.

Fig 6. Correlation between nuclear morphometric parameters extracted from RGB images and 5-DFS. Number (a), circularity (b), eccentricity (c), and major axis length (d) were negatively correlated with 5-DFS. The average area (e), average perimeter (f), and total area/total perimeter ratio (g) were positively correlated with 5-DFS. The average (area/perimeter) ratio (h) showed no correlation with 5-DFS.

Fig 7. ROC analyses on the prognostic value of nuclear morphometric and integrated features for 5-DFS. (a) Based on the analysis of MS images, integrated parameter 1 had a higher AUC than the other four parameters, and

integrated parameter 2 had a lower AUC than the other four parameters for predicting recurrence. (b) Similar results were further realized from the determination of HE RGB images.

Table 1. Clinicopathological characteristics of 134 CRC patients

Characteristics	N (%)	Recurrence n (%)	-DFS Rate (%)	*P*-value
Age (years)				0.141
≤ 65	74 (55.2)	32 (43.2)	56.8	
> 65	60 (44.8)	17 (28.3)	71.7	
Gender				0.116
Male	72 (53.7)	31 (43.1)	56.9	
Female	62 (46.3)	18 (29.0)	71.0	
Tumor site				0.473
Proximal colon	45 (33.6)	19 (42.2)	57.8	
Distal colon	39 (29.1)	13 (33.3)	66.7	
Rectum	50 (37.3)	17 (34.0)	66.0	
T stage				0.038
pT1/2	16 (11.9)	2 (12.5)	87.5	
pT3/4	118 (88.1)	47 (39.8)	60.2	
Histological grade				0.041
Well	46 (34.3)	15 (32.6)	67.4	
Moderate	59 (44.1)	19 (32.2)	67.8	
Poor	29 (21.6)	15 (51.7)	48.3	
LN status				< 0.001
Positive	53 (39.5)	38 (71.7)	28.3	
Negative	81 (60.5)	11 (13.6)	86.4	
Lymphovascular invasion				0.061
Yes	24 (17.9)	12 (50.0)	50.0	
No	110 (82.1)	37 (33.6)	66.4	
Clinical stage				< 0.001
I, II	79 (59.0)	13 (16.5)	83.5	

III, IV	55 (41.0)	36 (65.4)	34.6	
Adjuvant chemotherapy				0.703
Yes	76 (56.7)	29 (39.5)	61.8	
No	58 (43.3)	20 (32.7)	65.5	
Recurrence				N/A
Yes	49 (36.6)	N/A	N/A	
No	85 (63.4)	N/A	N/A	

Abbreviations: CRC, colorectal cancer; DFS, disease-free survival; LNs, lymph nodes; N/A, not available; T, tumor.

Table 2. Pixel-level quantitative evaluation of nuclei segmentation in HE-stained images

Image ID	Segmentation of MS images					Segmentation of RGB images				
	Accuracy (%)	Sensitivity (%)	Specificity (%)	Precision (%)	Dice index	Accuracy (%)	Sensitivity (%)	Specificity (%)	Precision (%)	Dice index
A	88.6	63.6	95.9	63.1	0.512	87.9	63.5	95.0	58.4	0.499
B	81.7	64.1	94.0	59.7	0.534	76.1	66.1	89.0	54.0	0.510
C	89.1	55.4	94.5	62.2	0.585	88.7	48.6	95.2	60.9	0.546
D	86.6	56.6	94.7	73.7	0.698	82.4	56.5	94.5	69.6	0.639
E	96.1	78.7	98.1	82.0	0.803	83.9	62.3	91.1	70.4	0.703
F	91.4	76.5	94.8	77.6	0.770	88.7	60.3	95.3	74.9	0.688
G	93.1	75.9	93.9	70.4	0.736	91.0	73.6	93.1	66.2	0.693
H	90.6	53.8	96.4	75.8	0.618	90.6	52.5	96.5	71.1	0.603
I	87.8	49.1	93.8	60.7	0.570	81.5	37.6	93.3	54.6	0.446
J	86.1	70.5	95.3	73.4	0.599	82.1	65.4	95.8	72.3	0.545
K	94.6	70.6	96.6	71.1	0.699	87.5	65.7	96.6	67.8	0.607
L	77.9	61.4	89.6	66.4	0.670	73.3	61.3	87.8	62.7	0.638
Average	88.6	64.7	94.8	69.7	0.650	84.5	59.4	93.6	65.2	0.593

Table 3. Nuclear parameters of MS images of CRC determined by computer-aided segmentation

Parameters	Results	Cut off points by X-tile		Grading		
	Median (range)	□/□	□/□	□	□	□
Number	620 (255-1082)	630	735	59	54	21
Circularity	0.61 (0.46-0.77)	0.62	0.65	72	36	26
Eccentricity	0.21 (0.05-0.36)	0.21	0.26	41	50	43
Major axis length	82.02 (60.42-147.58)	79.97	75.10	62	41	31
Average area	323.88 (276.47-419.80)	293.56	303.59	23	42	69
Average perimeter	84.76 (72.92-103.94)	80.45	83.37	14	36	84
Total area/total perimeter ratio	3.99 (3.07-6.47)	3.78	4.25	13	48	73
Average (area/perimeter) ratio	1.06 (0.89-1.39)	1.00	1.01	39	51	44

Table 4. Nuclear parameters of RGB images of CRC determined by computer-aided segmentation

Parameters	Results	Cut off values by X-tile		Grading		
	Median (range)	□/□	□/□	□	□	□
Number	598 (243.0-1068.0)	602	729	58	55	21
Circularity	0.60 (0.45-0.76)	0.60	0.64	68	43	23
Eccentricity	0.18 (0.03-0.32)	0.17	0.21	48	46	40
Major axis length	77.92 (58.32-138.47)	94.91	85.49	54	48	32
Average area	316.88 (264.01-416.48)	322.62	315.94	28	32	74
Average perimeter	84.35 (69.79-101.93)	79.57	87.66	15	35	84
Total (area/perimeter) ratio	3.90 (3.00-6.45)	3.60	4.20	13	57	64

Table 5. ROC analysis on nuclear morphometric parameters and integrated parameters 1 and 2

Parameters	HE MS images			HE RGB images		
	AUC	95% CI	*P*-value	AUC	95% CI	*P*-value
Number	0.746	0.660-0.832	< 0.001	0.736	0.649-0.824	< 0.001
Circularity	0.756	0.669-0.844	< 0.001	0.705	0.611-0.799	< 0.001
Eccentricity	0.669	0.575-0.762	0.001	0.651	0.555-0.747	0.004
Major axis length	0.661	0.563-0.759	0.002	0.653	0.555-0.751	0.003
Integrated parameter 1	0.785	0.700-0.870	< 0.001	0.773	0.691-0.855	< 0.001
Average area	0.283	0.190-0.376	< 0.001	0.334	0.235-0.433	0.001
Average perimeter	0.366	0.265-0.466	0.010	0.369	0.269-0.469	0.012
Total (area/perimeter)	0.372	0.271-0.472	0.014	0.386	0.285-0.487	0.028
Average (area/perimeter)	0.347	0.250-0.444	0.003	0.403	0.304-0.503	0.063
Integrated parameter 2	0.280	0.189-0.307	< 0.001	0.313	0.216-0.41000	< 0.001

Abbreviations: AUC, area under the curve; CI, confidence interval.

Table 6. Multivariate Cox proportional hazards model to predict 5-DFS in 134 CRC patients

Parameters	MS images			RGB images		
	Coefficient	HR (95% CI)	*P*-value	Coefficient	HR (95% CI)	*P*-value
T stage	0.392	1.479 (0.347-6.308)	0.597	0.239	1.270 (0.294-5.481)	0.748
LNs status	1.642	5.165 (2.529-10.550)	< 0.001	1.502	4.490 (2.204-9.149)	< 0.001
Histological grade	0.299	1.349 (0.920-1.978)	0.125	0.298	1.347 (0.897-2.025)	0.151
Integrated parameter 1	1.052	2.863 (2.014-4.070)	< 0.001	1.016	2.761 (1.881-4.052)	< 0.001
Integrated parameter 2	-1.020	0.361 (0.213-0.610)	< 0.001	-0.328	0.721 (0.511-1.015)	0.061
Clinical stage	0.899	2.457 (1.248-4.835)	0.009	1.088	2.968 (1.491-5.911)	0.002

Abbreviations: 5-DFS, 5-year disease-free survival; HR, hazard ratio; CI, confidence interval; T, tumor; LNs, lymph nodes.

Table 7. Prediction efficiency of nuclear integrated parameters for CRC prognosis

Parameters	Integrated parameter 1		Integrated parameter 2	
	MS images	RGB images	MS images	RGB images
Sensitivity (%)	75.5 (37/49)	63.3 (30/49)	53.1 (26/49)	42.8 (21/49)
Specificity (%)	77.6 (66/85)	75.3 (64/85)	85.9 (73/85)	77.6 (66/85)
PPV (%)	66.1 (37/56)	59.6 (31/52)	68.4 (26/38)	52.5 (21/40)
NPV (%)	84.6 (66/78)	78.0 (64/82)	76.0 (73/96)	70.2 (66/94)
Accuracy (%)	76.9 (103/134)*	70.9 (95/134)	73.9 (99/134)§	64.9 (87/134)

Abbreviations: PPV, positive predictive value; NPV, negative predictive value. *$p = 0.041$ compared with RGB images, 95% CI, 1.04-13.90%. §$p = 0.007$ compared with RGB images, 95% CI, 3.0-16.4%.

Reference

Bai B., Yang X., Li Y., Zhang Y., Pillar N. and Ozcan A. (2023). Deep learning-enabled virtual histological staining of biological samples. Light Sci. Appl. 12, 57.

Bosman F.T., Carneiro F., Hruban R.H. and Theise N.D. (2010). Who classification of tumours of the digestive system. World Health Organization.

Buchberger A.R., DeLaney K., Johnson J. and Li L. (2018). Mass spectrometry imaging: A review of emerging advancements and future insights. Anal. Chem. 90, 240-265.

Camp R.L., Dolled-Filhart M. and Rimm D.L. (2004). X-tile: A new bio-informatics tool for biomarker assessment and outcome-based cut-point optimization. Clin. Cancer Res. 10, 7252-7259.

Chaddad A., Tanougast C., Dandache A. and Bouridane A. (2011). Extracted haralick's texture features and morphological parameters from segmented multispectrale texture bio-images for classification of colon cancer cells. WSEAS Transactions on Biology and Biomedicine 8, 39-50.

Chen J.M., Qu A.P., Wang L.W., Yuan J.P., Yang F., Xiang Q.M., Maskey N., Yang G.F., Liu J. and Li Y. (2015). New breast cancer prognostic factors identified by computer-aided image analysis of he stained histopathology images. Sci. Rep. 5, 10690.

Dolens E.D.S., Dourado M.R., Almangush A., Salo T.A., Gurgel Rocha C.A., da Silva S.D., Brennan P.A. and Coletta R.D. (2021). The impact of histopathological features on the prognosis of oral squamous cell carcinoma: A comprehensive review and meta-analysis. Front. Oncol. 11, 784924.

Fereidouni F., Griffin C., Todd A. and Levenson R. (2018). Multispectral analysis tools can increase utility of RGB

color images in histology. J. Opt. 20, 044007.

Fischer A.H., Jacobson K.A., Rose J. and Zeller R. (2008). Hematoxylin and eosin staining of tissue and cell sections. CSH Protoc. 1:2008:pdb.prot4986.

Gao Y., Geras K.J., Lewin A.A. and Moy L. (2019). New frontiers: An update on computer-aided diagnosis for breast imaging in the age of artificial intelligence. AJR Am. J. Roentgenol. 212, 300-307.

Halicek M., Fabelo H., Ortega S., Callico G.M. and Fei B. (2019). In-vivo and ex-vivo tissue analysis through hyperspectral imaging techniques: Revealing the invisible features of cancer. Cancers (Basel) 11, 756.

He L., Long L.R., Antani S. and Thoma G.R. (2012). Histology image analysis for carcinoma detection and grading. Comput. Meth. Prog. Bio. 107, 538-556.

Hossain M.S., Karuniawati H., Jairoun A.A., Urbi Z., Ooi J., John A., Lim Y.C., Kibria K.M.K., Mohiuddin A.K.M., Ming L.C., Goh K.W. and Hadi M.A. (2022). Colorectal cancer: A review of carcinogenesis, global epidemiology, current challenges, risk factors, preventive and treatment strategies. Cancers (Basel) 14, 1732.

Hoyt C.C. (2021). Multiplex immunofluorescence and multispectral imaging: Forming the basis of a clinical test platform for immuno-oncology. Front. Mol. Biosci. 8, 674747.

Irshad H., Gouaillard A., Roux L. and Racoceanu D. (2014). Multispectral band selection and spatial characterization: Application to mitosis detection in breast cancer histopathology. Comput. Med. Imag. Graph. 38, 390-402.

Kaushal C., Islam M.K., Althubiti S.A., Alenezi F. and Mansour R.F. (2022). A framework for interactive medical image segmentation using optimized swarm intelligence with convolutional neural networks. Comput. Intell. Neurosci. 2022, 7935346.

Komura D. and Ishikawa S. (2018). Machine learning methods for histopathological image analysis. Comput. Struct. Biotechnol. J. 16, 34-42.

Kudo S.E., Mori Y., Abdel-Aal U.M., Misawa M., Itoh H., Oda M. and Mori K. (2021). Artificial intelligence and computer-aided diagnosis for colonoscopy: Where do we stand now? Transl. Gastroenterol. Hepatol. 6, 64.

Liang F., Wang S., Zhang K., Liu T.J. and Li J.N. (2022). Development of artificial intelligence technology in diagnosis, treatment, and prognosis of colorectal cancer. World J. Gastrointest. Oncol. 14, 124-152.

Liu W., Wang L., Liu J., Yuan J., Chen J., Wu H., Xiang Q., Yang G. and Li Y. (2016). A comparative performance analysis of multispectral and RGB imaging on HER2 status evaluation for the prediction of breast cancer

prognosis. Transl. Oncol. 9, 521-530.

Malshy K., Amiel G.E., Hershkovitz D., Sabo E. and Hoffman A. (2022). Association between nuclear morphometry parameters and gleason grade in patients with prostatic cancer. Diagnostics (Basel) 12, 1356.

Ortega S., Halicek M., Fabelo H., Callico G.M. and Fei B. (2020). Hyperspectral and multispectral imaging in digital and computational pathology: A systematic review [invited]. Biomed. Opt. Express. 11, 3195-3233.

Qu A., Chen J., Wang L., Yuan J., Yang F., Xiang Q., Maskey N., Yang G., Liu J. and Li Y. (2014). Two-step segmentation of hematoxylin-eosin stained histopathological images for prognosis of breast cancer. In: 2014 IEEE International Conference on Bioinformatics and Biomedicine (BIBM), 218-223. IEEE. pp 218-223.

Rathore S., Hussain M., Aksam Iftikhar M. and Jalil A. (2014). Ensemble classification of colon biopsy images based on information rich hybrid features. Comput. Biol. Med. 47, 76-92.

Rathore S., Iftikhar M.A., Chaddad A., Niazi T., Karasic T. and Bilello M. (2019). Segmentation and grade prediction of colon cancer digital pathology images across multiple institutions. Cancers (Basel) 11, 1700.

Siegel T., Hamm G., Bunch J., Cappell J., Fletcher J.S. and Schwamborn K. (2018). Mass spectrometry imaging and integration with other imaging modalities for greater molecular understanding of biological tissues. Mol. Imag. Biol. 20, 888-901.

Sirinukunwattana K., Pluim J.P.W., Chen H., Qi X., Heng P.A., Guo Y.B., Wang L.Y., Matuszewski B.J., Bruni E., Sanchez U., Böhm A., Ronneberger O., Cheikh B.B., Racoceanu D., Kainz P., Pfeiffer M., Urschler M., Snead D.R.J. and Rajpoot N.M. (2017). Gland segmentation in colon histology images: The glas challenge contest. Med. Image. Anal. 35, 489-502.

Sobin L.H., Gospodarowicz M.K. and Wittekind C. (2010). Tnm classification of malignant tumours. John Wiley & Sons.

Stegmaier J., Otte J.C., Kobitski A., Bartschat A., Garcia A., Nienhaus G.U., Strähle U. and Mikut R. (2014). Fast segmentation of stained nuclei in terabyte-scale, time resolved 3D microscopy image stacks. PLoS One 9, e90036.

Tani S., Fukunaga Y., Shimizu S., Fukunishi M., Ishii K. and Tamiya K. (2012). Color standardization method and system for whole slide imaging based on spectral sensing. Anal. Cell. Pathol. (Amst) 35, 107-115.

Veta M., van Diest P.J., Jiwa M., Al-Janabi S. and Pluim J.P. (2016). Mitosis counting in breast cancer: Object-level interobserver agreement and comparison to an automatic method. PLoS One 11, e0161286.

Wang L.W., Qu A.P., Liu W.L., Chen J.M., Yuan J.P., Wu H., Li Y. and Liu J. (2016). Quantum dots-based double imaging combined with organic dye imaging to establish an automatic computerized method for cancer Ki67 measurement. Sci. Rep. 6, 20564.

Wang W., Zhang X., Zhu L., Chen Y., Dou W., Zhao F., Zhou Z. and Sun Z. (2022). Prediction of prognostic factors and genotypes in patients with breast cancer using multiple mathematical models of mr diffusion imaging. Front. Oncol. 12, 825264.

Waterhouse D.J., Privitera L., Anderson J., Stoyanov D. and Giuliani S. (2023). Enhancing intraoperative tumor delineation with multispectral short-wave infrared fluorescence imaging and machine learning. J. Biomed. Opt. 28, 094804.

Wong M.C.S., Huang J., Lok V., Wang J., Fung F., Ding H. and Zheng Z.J. (2021). Differences in incidence and mortality trends of colorectal cancer worldwide based on sex, age, and anatomic location. Clin. Gastroenterol. Hepatol. 19, 955-966.e961.

Wu Y., Xu Z., Yang W., Ning Z. and Dong H. (2022). Review on the application of hyperspectral imaging technology of the exposed cortex in cerebral surgery. Front. Bioeng. Biotechnol. 10, 906728.

Xu Y., Jiang L., Chen W., Huang S., Liu Z. and Zhang J. (2023). Computer-aided detection and prognosis of colorectal cancer on whole slide images using dual resolution deep learning. J. Cancer Res. Clin. Oncol. 149, 91-101.

Zhang J., Su R., Fu Q., Ren W., Heide F. and Nie Y. (2022). A survey on computational spectral reconstruction methods from RGB to hyperspectral imaging. Sci. Rep. 12, 11905.

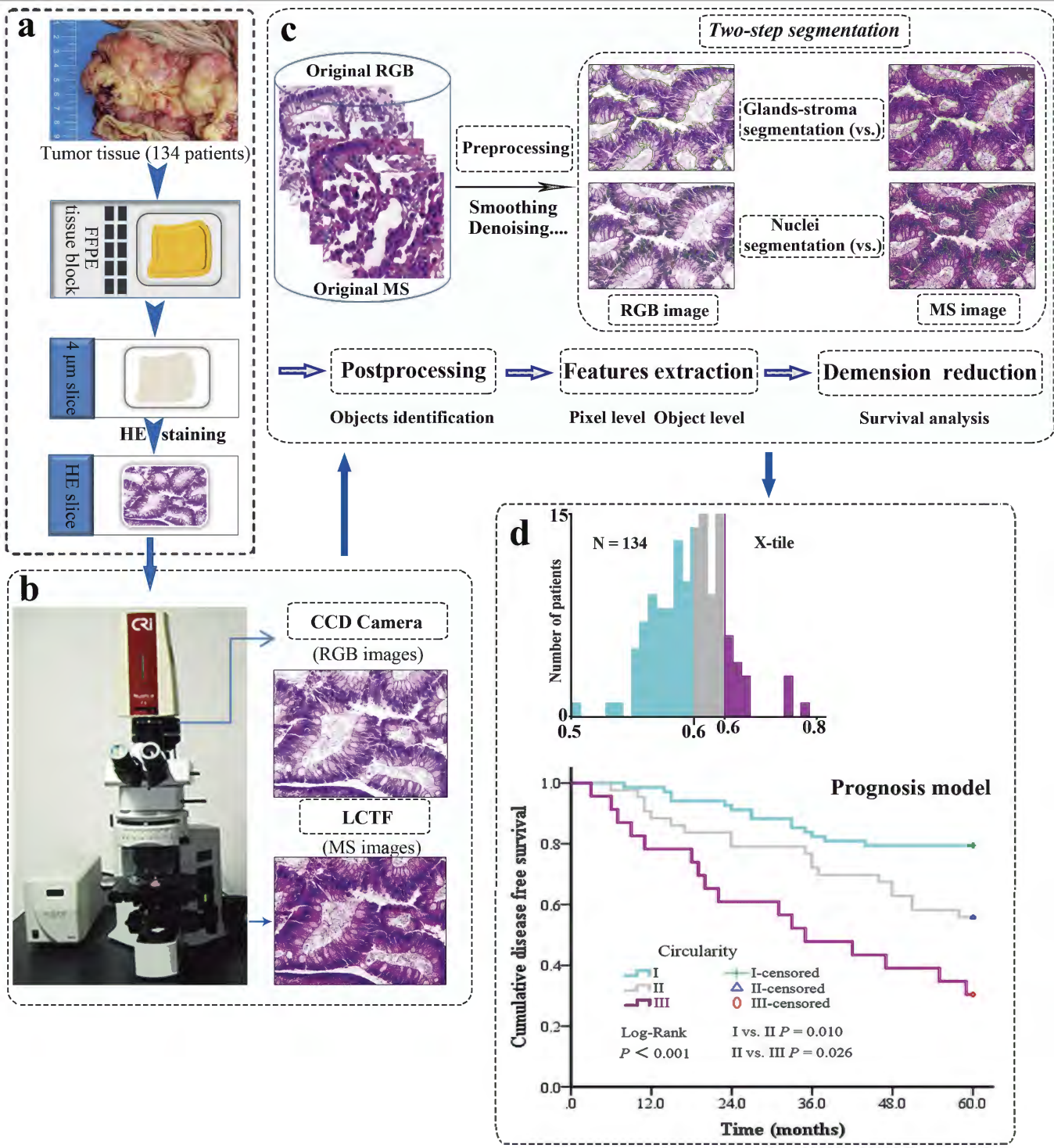
a
Tumor tissue (134 patients)
FFPE tissue block
4 μm slice
HE staining
HE slice
b
CCD Camera
(RGB images)
LCTF
(MS images)
c
Two-step segmentation
Original RGB
Original MS
Preprocessing
Smoothing
Denoising....
Glands-stroma segmentation (vs.)
Nuclei segmentation (vs.)
RGB image
MS image
Postprocessing
Features extraction
Demension reduction
Objects identification
Pixel level Object level
Survival analysis
d
N = 134
X-tile
Number of patients
15
0
0.5
0.6
0.6
0.8
Prognosis model
Cumulative disease free survival
1.0
0.8
0.6
0.4
0.2
0.0
Circularity
I
II
III
I-censored
II-censored
III-censored
Log-Rank
P < 0.001
I vs. II P = 0.010
II vs. III P = 0.026
0.0
12.0
24.0
36.0
48.0
60.0
Time (months)

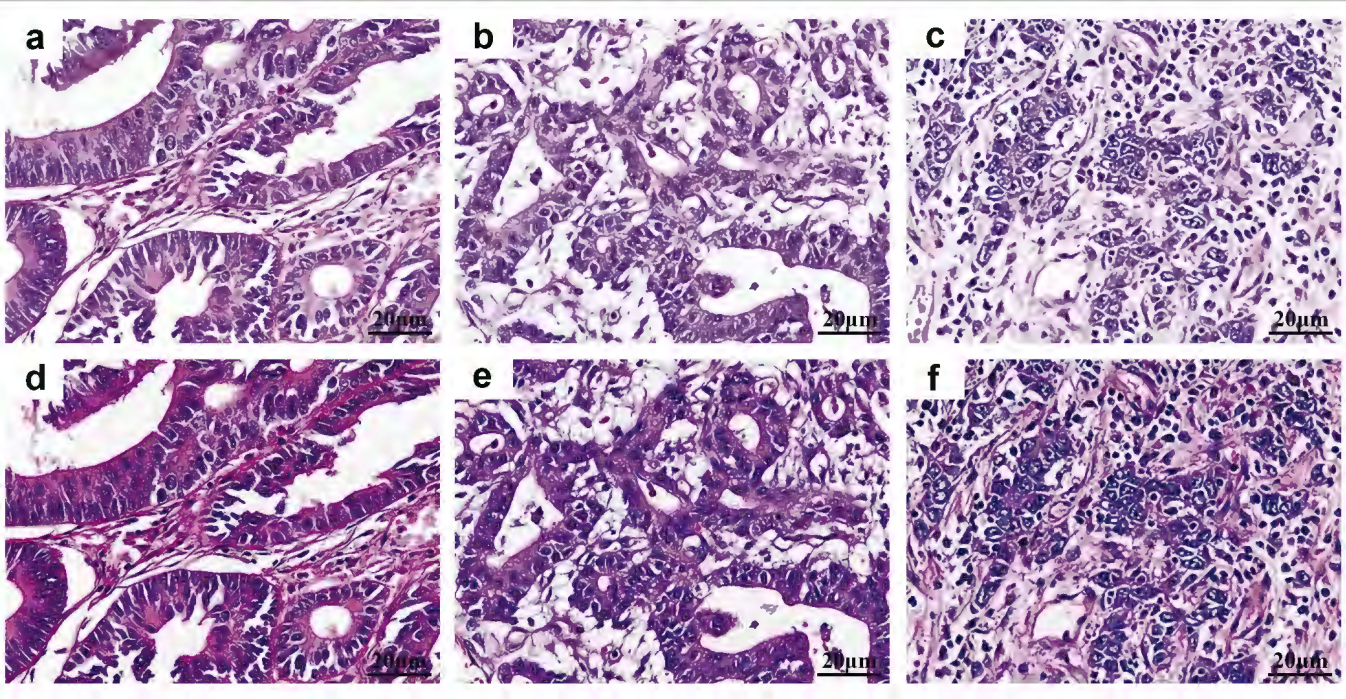
a
20μm
b
20μm
c
20μm
d
20μm
e
20μm
f
20μm

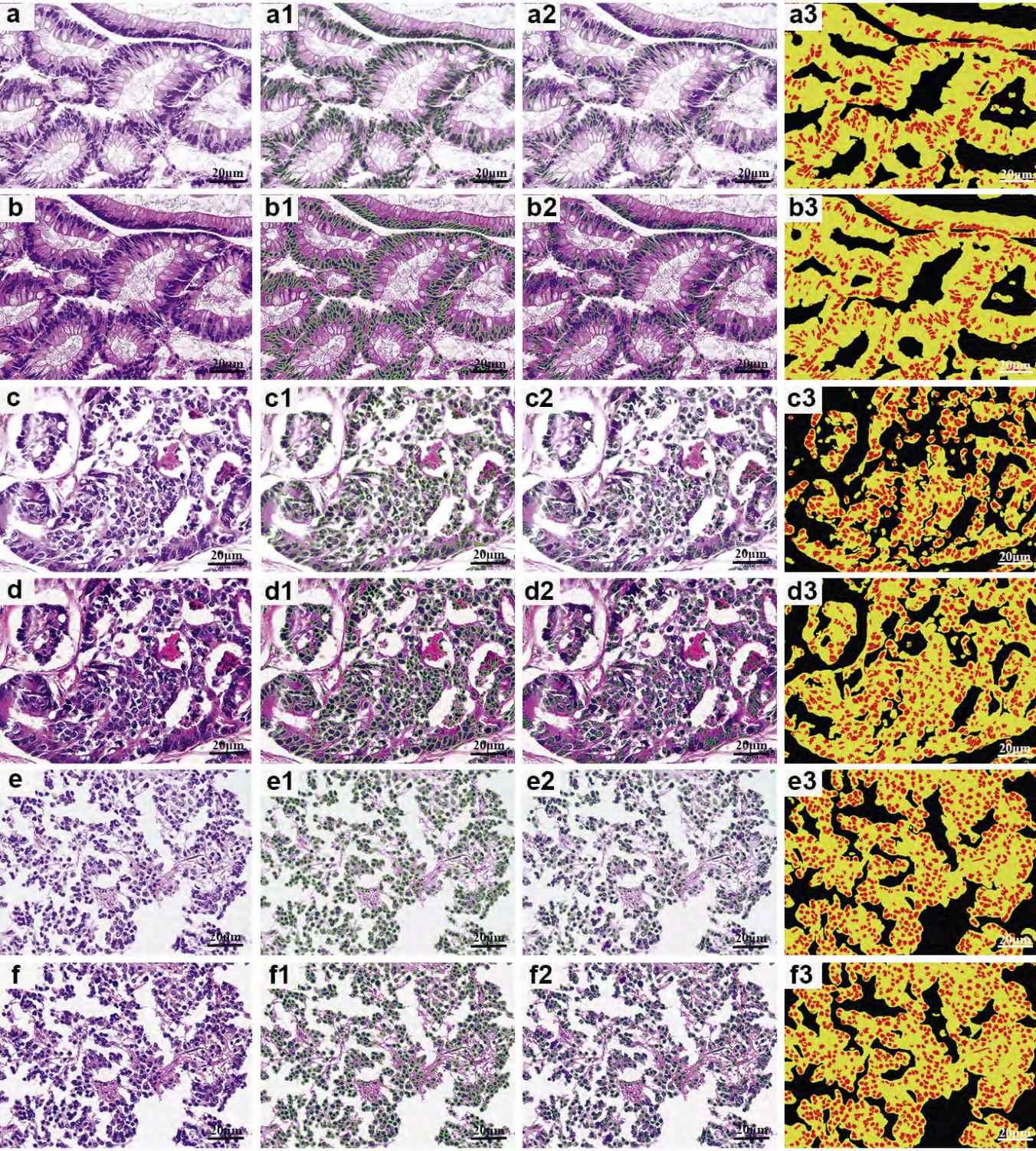
a
a1
a2
a3
b
b1
b2
b3
c
c1
c2
c3
d
d1
d2
d3
e
e1
e2
e3
f
f1
f2
f3
20μm

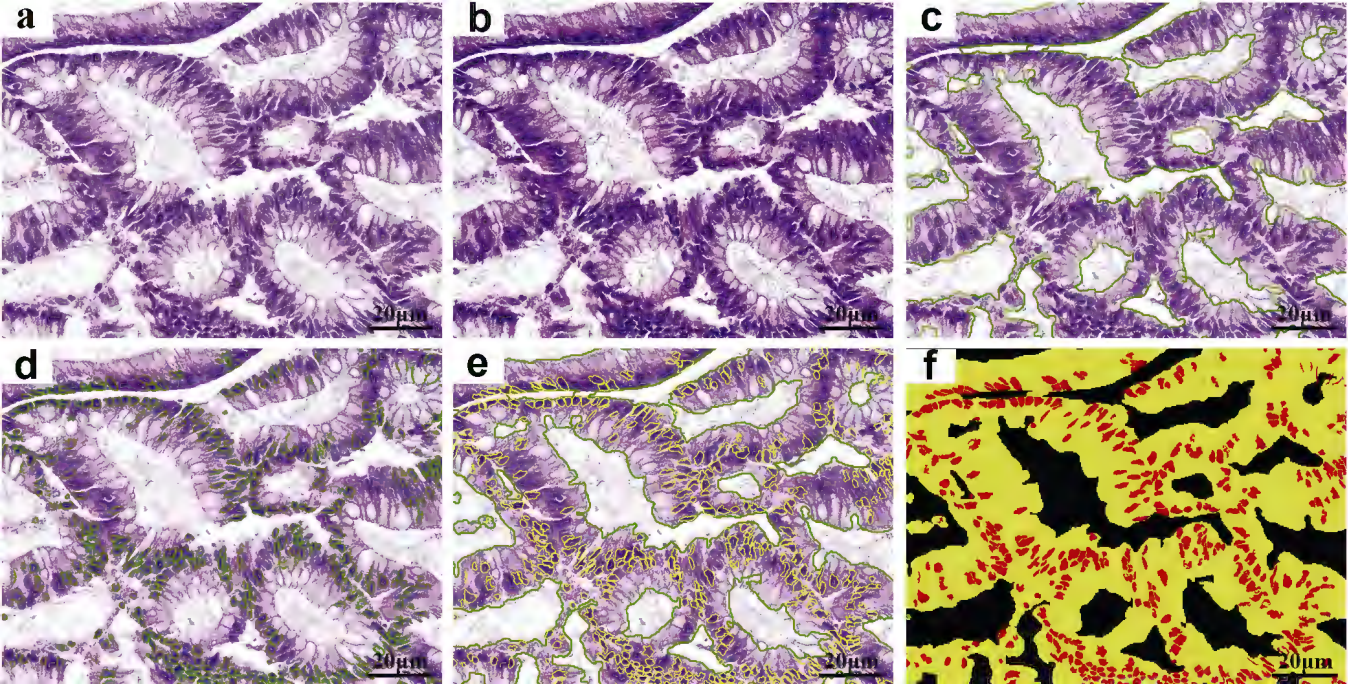
a
20μm
b
20μm
c
20μm
d
20μm
e
20μm
f
20μm

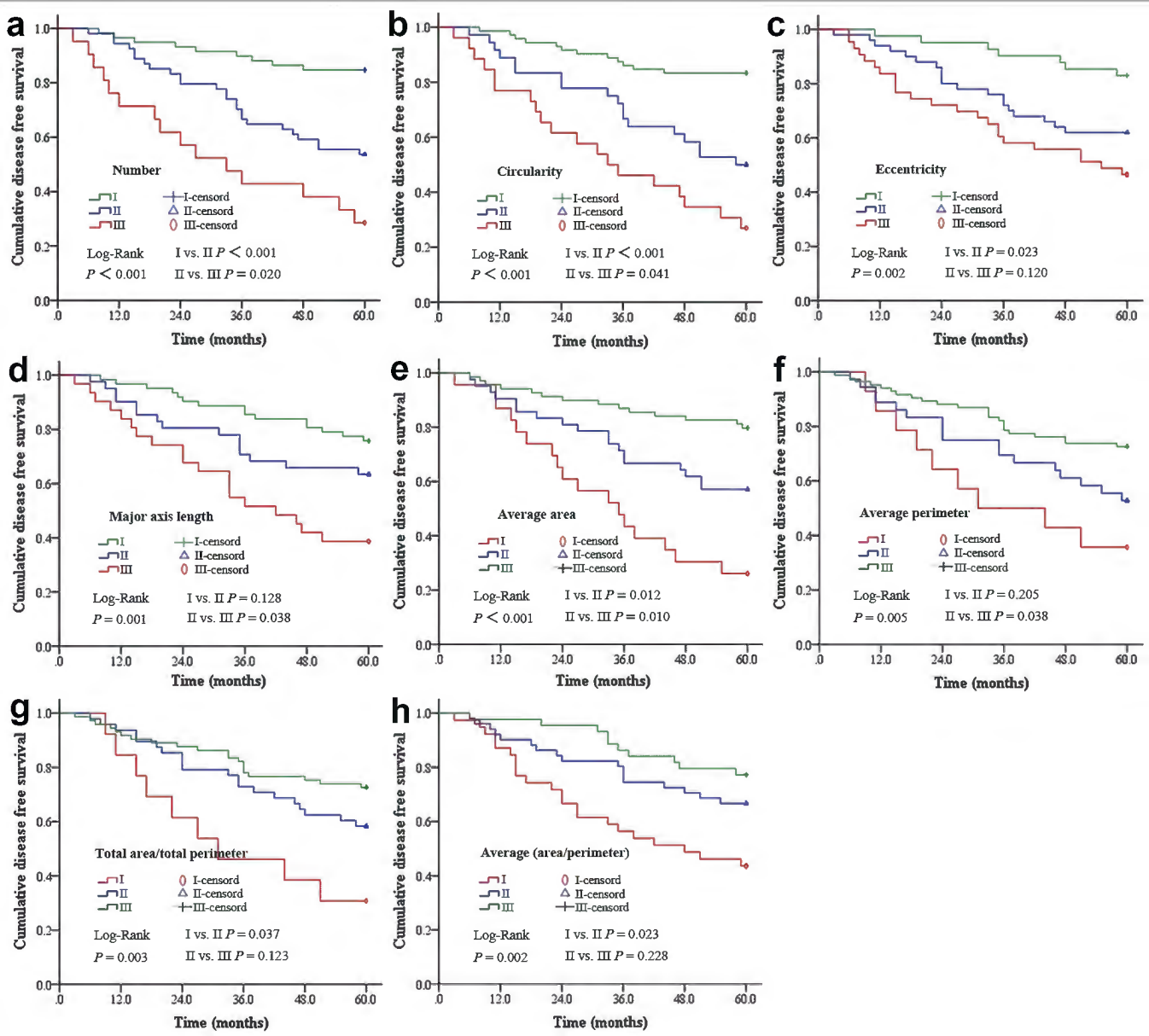
a
Cumulative disease free survival
Number
I
II
III
I-censord
II-censord
III-censord
Log-Rank
P < 0.001
I vs. II P < 0.001
II vs. III P = 0.020
Time (months)
b
Cumulative disease free survival
Circularity
I
II
III
I-censord
II-censord
III-censord
Log-Rank
P < 0.001
I vs. II P < 0.001
II vs. III P = 0.041
Time (months)
c
Cumulative disease free survival
Eccentricity
I
II
III
I-censord
II-censord
III-censord
Log-Rank
P = 0.002
I vs. II P = 0.023
II vs. III P = 0.120
Time (months)
d
Cumulative disease free survival
Major axis length
I
II
III
I-censord
II-censord
III-censord
Log-Rank
P = 0.001
I vs. II P = 0.128
II vs. III P = 0.038
Time (months)
e
Cumulative disease free survival
Average area
I
II
III
I-censord
II-censord
III-censord
Log-Rank
P < 0.001
I vs. II P = 0.012
II vs. III P = 0.010
Time (months)
f
Cumulative disease free survival
Average perimeter
I
II
III
I-censord
II-censord
III-censord
Log-Rank
P = 0.005
I vs. II P = 0.205
II vs. III P = 0.038
Time (months)
g
Cumulative disease free survival
Total area/total perimeter
I
II
III
I-censord
II-censord
III-censord
Log-Rank
P = 0.003
I vs. II P = 0.037
II vs. III P = 0.123
Time (months)
h
Cumulative disease free survival
Average (area/perimeter)
I
II
III
I-censord
II-censord
III-censord
Log-Rank
P = 0.002
I vs. II P = 0.023
II vs. III P = 0.228
Time (months)

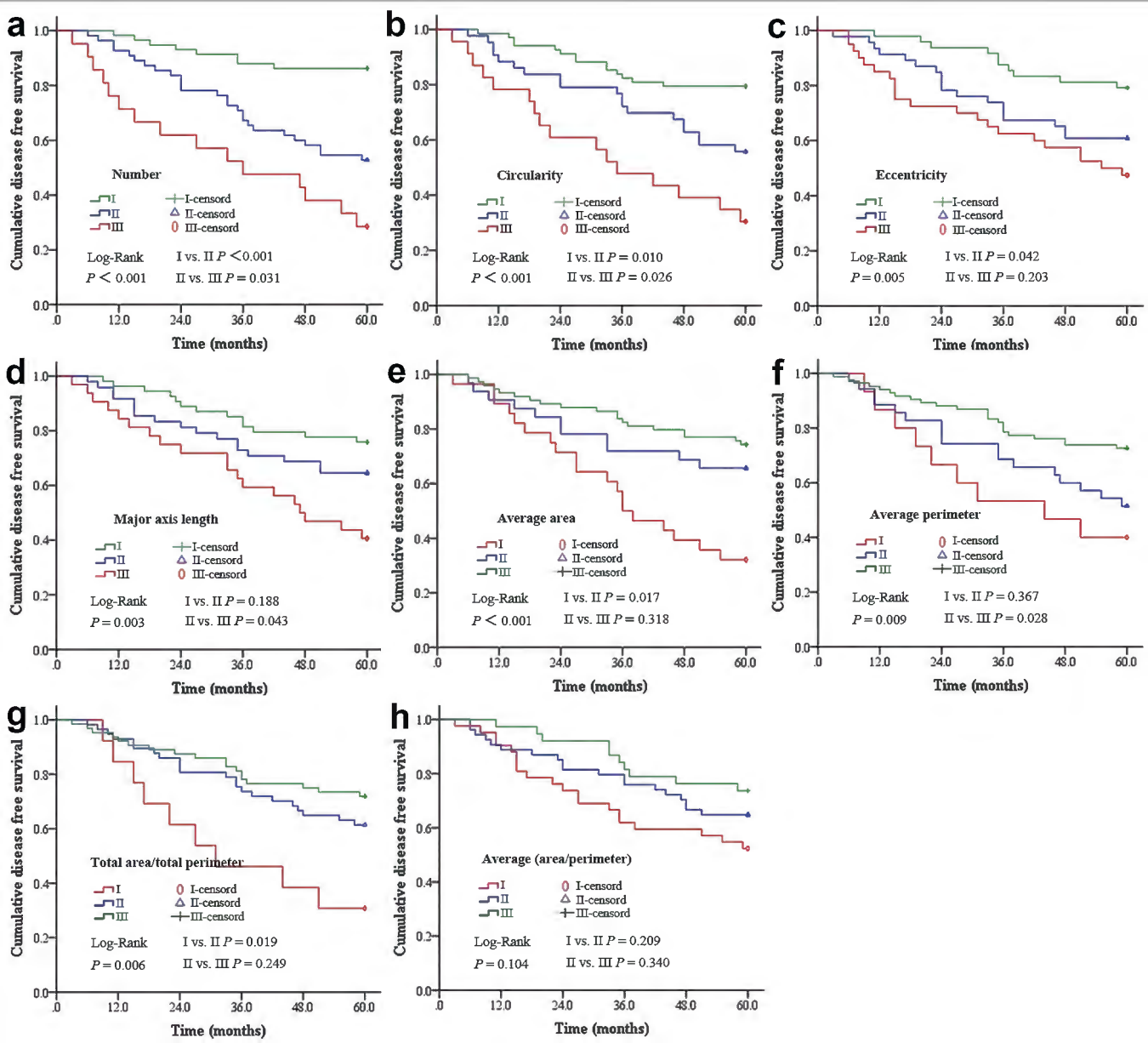
a
Cumulative disease free survival
Number
I
II
III
I-censord
II-censord
III-censord
Log-Rank
P < 0.001
I vs. II P <0.001
II vs. III P = 0.031
Time (months)
b
Cumulative disease free survival
Circularity
I
II
III
I-censord
II-censord
III-censord
Log-Rank
P < 0.001
I vs. II P = 0.010
II vs. III P = 0.026
Time (months)
c
Cumulative disease free survival
Eccentricity
I
II
III
I-censord
II-censord
III-censord
Log-Rank
P = 0.005
I vs. II P = 0.042
II vs. III P = 0.203
Time (months)
d
Cumulative disease free survival
Major axis length
I
II
III
I-censord
II-censord
III-censord
Log-Rank
P = 0.003
I vs. II P = 0.188
II vs. III P = 0.043
Time (months)
e
Cumulative disease free survival
Average area
I
II
III
I-censord
II-censord
III-censord
Log-Rank
P < 0.001
I vs. II P = 0.017
II vs. III P = 0.318
Time (months)
f
Cumulative disease free survival
Average perimeter
I
II
III
I-censord
II-censord
III-censord
Log-Rank
P = 0.009
I vs. II P = 0.367
II vs. III P = 0.028
Time (months)
g
Cumulative disease free survival
Total area/total perimeter
I
II
III
I-censord
II-censord
III-censord
Log-Rank
P = 0.006
I vs. II P = 0.019
II vs. III P = 0.249
Time (months)
h
Cumulative disease free survival
Average (area/perimeter)
I
II
III
I-censord
II-censord
III-censord
Log-Rank
P = 0.104
I vs. II P = 0.209
II vs. III P = 0.340
Time (months)

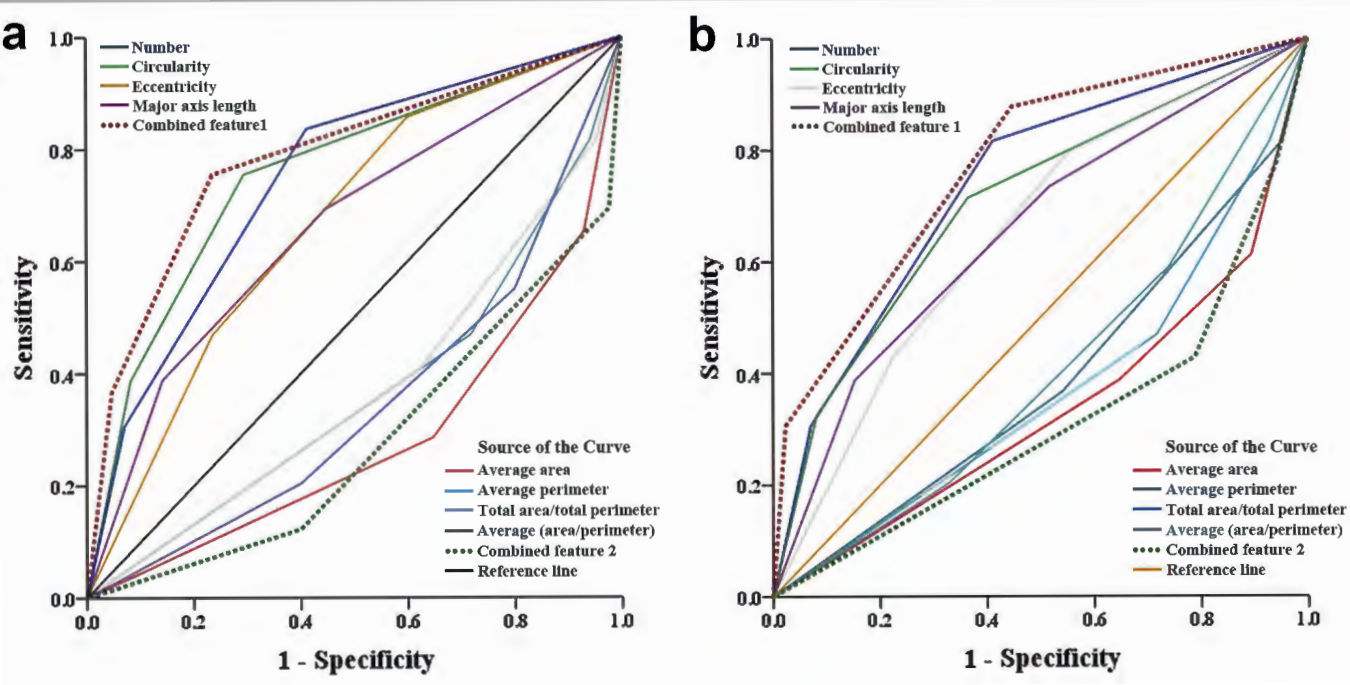
a
Number
Circularity
Eccentricity
Major axis length
Combined feature1
Source of the Curve
Average area
Average perimeter
Total area/total perimeter
Average (area/perimeter)
Combined feature 2
Reference line
Sensitivity
1 - Specificity
0.0
0.2
0.4
0.6
0.8
1.0
b
Number
Circularity
Eccentricity
Major axis length
Combined feature 1
Source of the Curve
Average area
Average perimeter
Total area/total perimeter
Average (area/perimeter)
Combined feature 2
Reference line
Sensitivity
1 - Specificity